REPORT DOCUMENTATION PAGE

Form Approved
OMB No. 0704-0188

1. REPORT DATE *(DD-MM-YYYY)*	**2. REPORT TYPE**	**3. DATES COVERED** *(From - To)*
June 2013	Technical Paper	June 2013-July 2013

4. TITLE AND SUBTITLE
Computational Investigation of Combustion Instabilities in a Laboratory-Scale LDI Gas Turbine Engine

5a. CONTRACT NUMBER
In-House

5b. GRANT NUMBER

5c. PROGRAM ELEMENT NUMBER

6. AUTHOR(S)
Yoon, C., Huang, C., Gejji, R., Anderson, W. and Sankaran, V.

5d. PROJECT NUMBER

5e. TASK NUMBER

5f. WORK UNIT NUMBER
Q12M

7. PERFORMING ORGANIZATION NAME(S) AND ADDRESS(ES)

Air Force Research Laboratory (AFMC)
AFRL/RQR
5 Pollux Drive
Edwards AFB CA 93524-7048

8. PERFORMING ORGANIZATION REPORT NO.

9. SPONSORING / MONITORING AGENCY NAME(S) AND ADDRESS(ES)
Air Force Research Laboratory (AFMC)
AFRL/RQR
5 Pollux Drive
Edwards AFB CA 93524-7048

10. SPONSOR/MONITOR'S ACRONYM(S)

11. SPONSOR/MONITOR'S REPORT NUMBER(S)
AFRL-RQ-ED-TP-2013-167

12. DISTRIBUTION / AVAILABILITY STATEMENT
Distribution A: Approved for Public Release; Distribution Unlimited. PA#13434

13. SUPPLEMENTARY NOTES
Conference paper for the 49th AIAA/ASME/SAE/ASEE Joint Propulsion Conference, San Jose, CA, 15-17 July 2013.

14. ABSTRACT
Self-excited combustion instabilities in a lean direct injection (LDI) gas turbine combustor are computationally investigated. The model LDI combustor under study was developed to produce combustion dynamics on demand using a single LDI element in an axisymmetric combustor. Three simulation cases for this combustor are considered: non-reacting and reacting flow in an acoustically open combustor and reacting flow in an acoustically closed combustor. We studied the dynamic flow features in the LDI combustor for both cases and investigated the important modes using a dynamic mode decomposition method. Precessing vortex core (PVC) instabilities are indicated as the critical hydrodynamic mode and lead to strong spray and flame response. In the acoustically close chamber simulation, we were able to capture self-excited combustion instabilities and the dominant modes from simulations, which qualitatively agree with the experimental results. The appearance of pressure peaks in both simulation and experiment at about 1400 Hz corresponding to the 4L acoustic mode and at 6000 Hz are explained by the nonlinear coupling of the PVC and acoustics modes and the associated feedback loop.

15. SUBJECT TERMS

16. SECURITY CLASSIFICATION OF:			**17. LIMITATION OF ABSTRACT**	**18. NUMBER OF PAGES**	**19a. NAME OF RESPONSIBLE PERSON**
					Venkateswaran Sankaran
a. REPORT	**b. ABSTRACT**	**c. THIS PAGE**	SAR	19	**19b. TELEPHONE NO** *(include area code)*
Unclassified	**Unclassified**	**Unclassified**			661-525-5534

Standard Form 298 (Rev. 8-98)
Prescribed by ANSI Std. 239.18

Computational Investigation of Combustion Instabilities in a Laboratory-Scale LDI Gas Turbine Engine

Changjin Yoon[1], Cheng Huang[2], Rohan Gejji[3] and William E. Anderson[4]
Maurice J. Zucrow Laboratories, Purdue University, West Lafayette, IN, 47906

and

Venkateswaran Sankaran[5]
Air Force Research Laboratory, Edwards AFB, CA, 93524

Self-excited combustion instabilities in a lean direct injection (LDI) gas turbine combustor are computationally investigated. The model LDI combustor under study was developed to produce combustion dynamics on demand using a single LDI element in an axisymmetric combustor. Three simulation cases for this combustor are considered: non-reacting and reacting flow in an acoustically open combustor and reacting flow in an acoustically closed combustor. We studied the dynamic flow features in the LDI combustor for both cases and investigated the important modes using a dynamic mode decomposition method. Precessing vortex core (PVC) instabilities are indicated as the critical hydrodynamic mode and lead to strong spray and flame response. In the acoustically close chamber simulation, we were able to capture self-excited combustion instabilities and the dominant modes from simulations, which qualitatively agree with the experimental results. The appearance of pressure peaks in both simulation and experiment at about 1400 Hz corresponding to the 4L acoustic mode and at 6000 Hz are explained by the nonlinear coupling of the PVC and acoustics modes and the associated feedback loop.

I. Introduction

Lean Direct Injection (LDI) is a promising design concept in gas turbine engines. It was developed as a low NOx alternative to Lean Prevaporized Premixed (LPP) combustion for aircraft gas turbines. In the LPP design, the fuel droplets are atomized and pre-mixed with the air in a tube upstream of the combustor. Although this design can provide low NOx emissions due to the uniformly low equivalence ratio, the inherent auto-ignition and flashback are risks that may be too high for flight applications. On the other hand, in LDI combustors, the liquid fuel is rapidly dispersed by a highly inertial air flow and directly injected into the flame zone. While the issues of concern in the LPP design are nearly eliminated, NOx performance is compromised due to the absence of the premixing and prevaporization processes. The key for improved NOx performance in a LDI design therefore lies in good atomization and quick and uniform mixing.

Combustion dynamics introduce additional technical challenges to the design of low NOx combustors, and the vulnerability of the LDI design to self-excited pressure oscillations is well documented. [1, 2] As the combustion occurs under a lean premixed condition, the flame surface can be more responsive to acoustic fluctuations than a typical diffusion flame. The sensitivity of the chemical kinetics is also influenced by operation at low equivalence ratios. Lastly, the acoustic waves may be less damped due to the absence of significant vorticity generation across the orifices in the LDI design.

---

[1] Postdoctoral Researcher, School of Aeronautics and Astronautics and Member AIAA.
[2] Graduate Research Assistant, School of Mechanical Engineering and Student Member AIAA.
[3] Graduate Research Assistant, School of Mechanical Engineering and Student Member AIAA.
[4] Professor, School of Aeronautics and Astronautics and Associate Fellow AIAA.
[5] Senior Scientist, Rocket Propulsion Division and Senior Member AIAA.

This study is aimed at analyzing combustion dynamics in a laboratory LDI combustor and enhancing our understanding of the underlying driving mechanisms by means of a high-fidelity simulations and companion experimental tests. A single-element LDI model combustor which generates self-excited pressure oscillations was developed for the present study. The computational simulation considers two different geometries: acoustically-open and acoustically-closed combustors. The acoustically-open combustor allows the study of inherent hydrodynamics and heat release without the influence of acoustics. In addition to reacting flow simulations in these two combustors, we non-reacting flow in the acoustically-open geometry is also studied in order to understand the change of flow characteristics due to chemical reactions and longitudinal acoustics. The major mode shapes due to the hydrodynamic instabilities are investigated using Dynamic Mode Decomposition (DMD). Lastly, the combustion dynamics in the LDI combustor are estimated by the computational simulation and a physical interpretation of the simulation results is provided to help understand the underlying combustion dynamics mechanisms.

II. Computational Model Description

A. Computational Framework (GEMS)

The computational platform for the present simulations is the in-house research code GEMS (General Equation and Mesh Solver).[3, 4] GEMS is a fully unstructured, density-based finite volme solver with a second-order numerical scheme and an implicit, dual time procedure for time-accuracy. The capabilities of the code for capturing the combustion dynamics and predicting self-excited instabilities have been successfully demonstrated for rocket engine combustors.[5-7] GEMS solves the Navier-Stokes equations in Detached Eddy Simulations (DES) mode along with the continuity, energy and species equation described below.

$$\frac{\partial Q}{\partial t} + \nabla \cdot \left(F - F_v \right) = S \tag{1}$$

where the conservative variables, Q, inviscid and viscous flux vectors, F and F_v, and source term vector, S, are given by

$$Q = \begin{pmatrix} \rho \\ \rho \mathbf{Y} \\ \rho \mathbf{V} \\ \rho h^0 - p \\ \rho \mathbf{K} \end{pmatrix}, \quad F = \begin{pmatrix} \rho \mathbf{V}^T \\ \rho \mathbf{Y} \mathbf{V}^T \\ \rho \mathbf{V} \mathbf{V}^T + p\bar{I} \\ \rho h^0 \mathbf{V}^T \\ \rho \mathbf{K} \mathbf{V}^T \end{pmatrix}, \quad F_v = \begin{pmatrix} 0 \\ \rho D \nabla \mathbf{Y} \\ \bar{\tau} \\ \bar{\tau} \cdot \mathbf{V} - q \\ \mu_K \nabla \mathbf{K} \end{pmatrix} \quad \text{and} \quad S = \begin{pmatrix} 0 \\ \dot{\omega} \\ 0 \\ 0 \\ s_K \end{pmatrix} + S_L \tag{2}$$

The quantities; ρ, $\mathbf{V}$ and p represent the density, velocity vector and pressure respectively; h^0 is the stagnation enthalpy and $\mathbf{Y}$ is a species mass fraction vector; $\mathbf{K}$ represents the turbulence variable vector which includes turbulence kinetic energy and specific dissipation, k and w; In the viscous flux, D is the molecular diffusion coefficient; τ is the stress tensor and q is the heat flux; w and s_K are the reaction rate and sources of the turbulence transport equations respectively. A pseudo-time term expressed in terms of the primitive variables, $Q_p = \begin{bmatrix} \rho & \mathbf{Y} & \mathbf{V} & T & \mathbf{K} \end{bmatrix}^T$ and a preconditioning matrix, Γ, is added to Eq. (1), so that the equation becomes:

$$\Gamma \frac{\partial Q_p}{\partial \tau} + \frac{\partial Q}{\partial \tau} + \nabla \cdot \left(F - F_v \right) = 0 \tag{3}$$

The matrix, Γ, is chosen to control the artificial disspation in the spatial discretization and the convergence of the pseudo-time iterations. The preconditioning matrix, Γ, in the pseudo time term in Eq. (3) is defined by starting from the Jacobian of the conservative variables with respect to the primitive variables, $\partial Q / \partial Q_p$, as shown below:

$$\Gamma = \begin{pmatrix} \rho_p & \rho_{\mathbf{Y}} & 0 & \rho_T & 0 \\ \rho_p \mathbf{Y} & \rho_{\mathbf{Y}} \mathbf{Y} + \rho & 0 & \rho_T \mathbf{Y}^T & 0 \\ \rho_p \mathbf{V} & \rho_{\mathbf{Y}} \mathbf{V} & \rho \bar{\mathbf{I}} & \rho_T \mathbf{V}^T & 0 \\ \rho_p h^0 - \left(1 - \rho h_p \right) & \rho_{\mathbf{Y}} h^0 + \rho h_{\mathbf{Y}} & \rho \mathbf{V}^T & \rho_T h^0 + \rho h_T & 0 \\ \rho_p \mathbf{K} & \rho_{\mathbf{Y}} \mathbf{K} & 0 & \rho_T \mathbf{K} & \rho \end{pmatrix} \tag{4}$$

The flux formulation for a generalized upwind finite volume approach can be interpreted as the average of the fluxes on either side of the cell interfaces augmented by an artificial dissipation term,

$$\tilde{F} = \frac{1}{2}\left(F_L + F_R\right) - \frac{1}{2}\left|A\right|\left(Q_R - Q_L\right) = \frac{1}{2}\left(F_L + F_R\right) - \frac{1}{2}\Gamma\left|\Gamma^{-1}A_p\right|\left(Q_{pR} - Q_{pL}\right) \tag{5}$$

where the subscripts *R* and *L* represent values on the right and left side of the cell face. The numerical procedure uses a second-order approximate Riemann solver to evaluate the spatial fluxes at cell faces. Second-order temporal accuracy is achieved by means of an implicit dual time procedure that eliminates factorization and linearization errors.

B. Turbulence Model

The present simulations describe the large-scale, time-dependent turbulence motion by means of a Detached Eddy Simulation (DES) model.[8, 9] DES is a hybrid RANS/LES approach which combines the RANS method in the attached boundary layers with the LES method for the large separated and wake regions. A DES model can be obtained from any RANS model based on a local length-scale definition and our DES formulation uses the k-omega two equation model with the appropriate modification. This modification relies on the local turbulence length scale and the local grid dimensions to enable the switching from the RANS to LES mode. It activates the RANS mode near the solid surfaces where the flow is attached, whereas it invokes the LES mode in separated flow regions by reducing the dissipation term in turbulent kinetic energy transport equations. Specifically, the DES model replaces the length scale with the minimum of the length scale defined in turbulence model for RANS and maximum spacing of the local grid as:

$$l_{DES} = \min\left(l_{k-\omega}, C_{DES}\delta\right) \tag{6}$$

where $\delta = \max\left(\Delta x, \Delta y, \Delta z\right)$ represents the maximum grid spacing in any direction and C_{DES} is a model constant and set equal to 0.78 as recommended by Travin et al.; $l_{k-\omega}$ is the length scale of Wilcox's k-w two equation model for the turbulence closure in RANS and it is defined as

$$l_{k-\omega} = \frac{k^{1/2}}{\beta^*\omega} \tag{7}$$

where β^* is a model constant. This definition of the length scale by Eq. (6) ensures the RANS mode is utilized near the wall surface in which the high grid apect ratio is typically expected. Finally, the dissipation term in the transport equation of the turbulence kinetic energy is replaced by

$$\beta^*\rho k w = \frac{\rho k^{3/2}}{l_{DES}} \tag{8}$$

This modification ensures that the resulting sub-grid model reduces to a Smagorinky-like model at equilibrium.

C. Combustion Model

The two-step global reduced mechanism by Westbrook is considered in the present study.[10] All six chemical species, $C_{12}H_{23}$, O_2, CO_2, H_2O, CO and N_2, are solved directly and turbulence transport in the species equations is modeled using the classical gradient model with a constant Schmidt number. Flamelet and transported FMDF models are popular in unsteady LES simulations, but their capabilities for combustion/acoustic interaction problems are not well-established. Laminar finite rate chemistry model is therefore used here, which solves transport equations for the chemical species, and uses Arrhenius rate expressions to describe the reaction rate. No additional turbulence-chemistry interactions are considered.

We consider the fuel as kerosene ($C_{12}H_{23}$) to approximate the experimental Jet-A fuel. A simplified two-step, five species global reduced mechanism has been incorporated in the present study.

$$2\mathbf{C_{12}H_{23}} + 35\mathbf{O_2} \longrightarrow 24\mathbf{CO} + 23\mathbf{H_2O}$$

$$2\mathbf{CO} + \mathbf{O_2} \longleftrightarrow 2\mathbf{CO_2}$$

The kinetics of the two-step global reactions are represented by an Arrhenius function of the form as:

$$\dot{\omega} = AT^n\left(-E_a / R_u T\right)\left[\mathbf{X_A}\right]^a\left[\mathbf{X_B}\right]^b \tag{9}$$

where w is the production rate, *A* is the pre-exponential constant, E_a is the activation energy, and *n*, *a* and *b* are exponents, respectively. For the first $C_{12}H_{23}$ oxidation step, the production rate is expressed with constants as $2.643\times10^9\exp(-1.5108\times10^4/T)[C_{12}H_{23}]^{0.25}[O_2]^{1.5}$. For the second step, it is expressed as $2.2387\times10^{12}\exp(-2.0143\times10^4/T)[CO][O_2]^{0.25}[H_2O]^{0.5}$ for the forward CO oxidation reaction, and as $5.0\times10^8\exp(-2.0143\times10^4/T)[CO_2]$ for the reverse CO dissociation reaction.

D. Lagrangian Phase Equations

The Lagrangian formulation for the liquid particle motion is expressed as a set of ordinary differential equations for the Larangian solution variables, Q_L, as:

$$\frac{dQ_L}{dt} = \frac{d}{dt}\begin{pmatrix} \mathbf{X} \\ \mathbf{U} \\ T_l \\ m_l \\ r \end{pmatrix} = \begin{pmatrix} \mathbf{U} \\ F_D\left(\mathbf{V}-\mathbf{U}\right) \\ \dot{m}_v\left[c_p\left(T_g - T_l\right) - L_v\right] / m_l C_l \\ -\dot{m}_v \\ -\dot{m}_v / \left(4\pi r^2\right) \end{pmatrix} \tag{10}$$

where **X**, **U**, T_l, m_l and r are the components of the Largrangian solution vector and these variables represent the position and velocity vector, temperature, mass and radius of the liquid particle respectively. The first and second rows represent the motion of particle droplets, where the drag is considered as an external force. In the source of second row, F_D is a drag parameter defined as $F_D = \frac{3}{8}\frac{C_D}{r}\frac{\rho_g}{\rho_l}\left|\mathbf{U}-\mathbf{V}\right|$ in which **V** is the carrier gas velocity vector and the drag coefficient follows Putnam's formulation based on a spherical drop assumption. [11]

$$C_D = \begin{cases} 0.44 & \mathrm{Re} < 1000 \\ \dfrac{24}{\mathrm{Re}}\left(1 + \dfrac{1}{6}\mathrm{Re}^{2/3}\right) & \mathrm{Re} > 1000 \end{cases} \tag{11}$$

Here, the Reynolds number, Re, is defined as $\frac{\rho_g d}{\mu_g}\left|\mathbf{U}-\mathbf{V}\right|$. The third row in Eq. (10) resprents the energy equation for the liquid particle. This equation assumes a uniform temperature inside the liquid particle. The source term consists of the net sensible enthalpy transfer, $c_p\left(T_g - T_l\right)$, and the latent heat of vaporization, L_v, and $m_l C_l$ represents the heat capacity of the liquid particle. The fourth row accounts for the mass balance during vaporization. The corresponding source term is the vaporization rate, $\dot{m}_v$, which is evaluated by means of the classical D^2-law:

$$\dot{m}_v = -2\pi r \rho_g D_s \mathrm{Sh} \ln\left(1 + B_M\right) \tag{12}$$

where D_s is a diffusion coefficient at the liquid surface and Sh is a Sherwood number; B_M is the Spalding mass transfer number [12] given by

$$B_M = \frac{Y_{F,s} - Y_{F,\infty}}{1 - Y_{F,s}} \tag{13}$$

where Y_F is the fuel species, subscripts s and ∞ indicate the surface and far field respectively. The last row accounts for the liquid particle radius reduction due to vaporization.

The set of Lagrangian phase equations, Eq. (10), is integrated explicitly and the Lagrangian time step is determined by consideration of the time scales of the particle lifetime, atomization initiation time and Eulerian time step, etc. All other physical properties of the liquid particle are updated every time step as well.

E. Injection and Atomization Model

The atomizer used in this study is a pressure swirl atomizer. The hollow cone fuel spray is described by the injection of a series of discrete liquid parcels which contain a bunch of drops. This parcel (or "blob") is the particle solved by the Lagrangian phase equations. Note the parcel is not an actual drop, but rather a cloud which contains a number of drops. The parcel undergoes a series of complicated physical processes, which are described by corresponding submodels as shown in Table 1. As shown in Figure 1, three main events are considered in the present model: free surface flow, primary atomization, and secondary atomization. Before forming the parcel, there is a free surface flow inside of the pressure swirl atomizer. Depending on the flow conditions and atomizer geometry, the liquid sheet thickness at the atomizer exit can be determined by Ibrahim and Jog's numerical model [13]. The liquid sheet around the atomizer exit disintegrates into ligaments and is subsequently broken into multiple droplets. This primary atomization process is described by Senecal et al's Linearized Instability Sheet Instability (LISA) model [14]. Furthermore, droplets from the primary atomization encounter aerodynamic forces due to the

strong swirling air flow, leading to variety of secondary atomization modes depending on the Weber number as shown in Table 1.

Table 1 Summary of Fuel Spray Modeling

Physical Process	Model	Results
Atomizer Free-Surface Flow	Ibrahim and Jog's Numerical Model [13]	Liquid sheet thickness Spray angle Sheet velocity
Primary Atomization	Senecal et al.'s Linearized Sheet Instability Atomization Model [14]	Ligament size Droplet size
Secondary Atomization - Vibration mode: 0<We<11 - Bag mode: 11<We<35 - Multimode: 35<We<80 - Sheet-thinning: 80<We<350 - Catastrophic mode: We>350	Hybrid TAB/KH/RT Model - No breakup: 11<We<35 - TAB Model: 11<We<35 - TAB/KH Model: 35<We<80 - KH Model: 80<We<350 - KH/RT Model: We>350	Droplet size

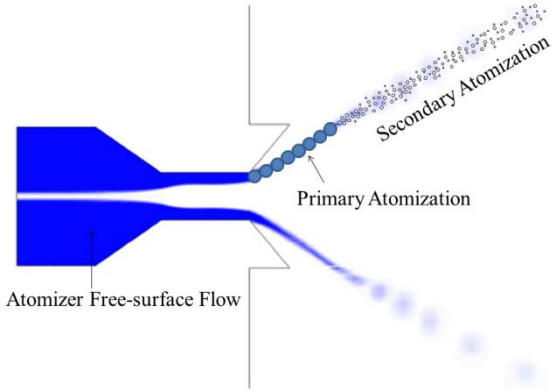

Figure 1 Modeling Schematics of High Pressure Fuel Spray

1. *Primary Atomization*

The primary atomization of hollow cone spray is accounted for by the LISA model, which determines the ligament size based on the most unstable wave length based on a linear instability analysis. The LISA model defines a dispersion relation between the disturbance growth rate, ω, and wave number, k, which are obtained by linearzing the liquid continuity and momentum equations as:

$$\omega^2\left[\tanh(kh)+Q\right]+\omega\left[4\nu_1k^2\tanh(kh)+2iQkU\right]+4\nu_1^2k^4\tanh(kh)$$
$$-4\nu_1^2k^3\tanh(kh)-QU^2k^2+\frac{\sigma k^3}{\rho_1}=0 \tag{14}$$

where h, Q, ρ_1, U and ν_1 are the liquid sheet thickenss, gas to liquid density ratio, liquid density, sheet velocity and liquid viscosity respectively. The dispersion equation is solved with a specified liquid sheet thickness, velocity and fuel properties by using the so-called golden-search method to obtain the maximum instability growth rate and the corresponding wavelength. This wavelength is used to define the ligament size as:

$$d_L=\sqrt{\frac{16h}{K_s}} \tag{15}$$

Based on Weber's column theory, the droplet size that breaks away from the ligament is determined as:

$$d_D=1.88d_L\left(1+3Oh\right)^{1/6} \tag{16}$$

Physically, complex multiphase processes are involved during this primary atomization event including the liquid sheet breakup into ligaments and ligament breakup into droplets. All these processes are computationally simplified and coupling with the surrounding gas is neglected to prevent any inaccurate physical interactions. The primary breakup time is determined empirically as:

$$\tau = \frac{1}{\Omega_s} \ln\left(\frac{\eta_b}{\eta_0}\right) \tag{17}$$

2. Secondary Atomization

Secondary atomization is modeled by means of a hybrid model that combines the Taylor Analogy Breakup (TAB) [15], Reitz's Kelvin-Helmholtz (KH) and Rayleigh-Taylor (RT) models [16-18]. Depending on the Weber number, there are distinct breakup modes during the secondary atomization. The hybrid model adaptively applies the appropriate submodel corresponding to the physical breakup mode. Among the submodels, the TAB model describes the bag breakup mode, which provides good accuracy for Weber numbers in the range of 11<We<35. On the other hand, the KH model represents the sheet-thinning mode (or stripping mode) that is suitable for 80<We<350 and produces a reasonable number of broken child parcels, thereby providing a continuous vaporized fuel. The transition between the bag-breakup and sheet-thinning modes occurs at 35<We<80 and we empirically determined the critical Weber number, We_c, to be 40 in the present simulations. Lastly, for even higher Weber numbers, RT instability is found to occur, which is driven by drop acceleration due to aerodynamic drag.

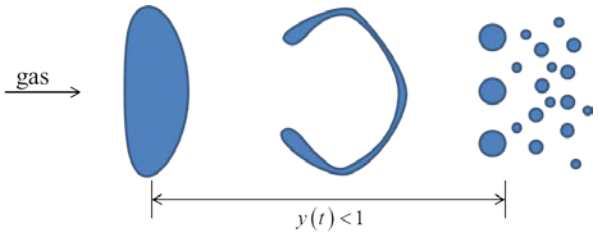

(a) TAB model for a bag breakup mode: 11<We<35

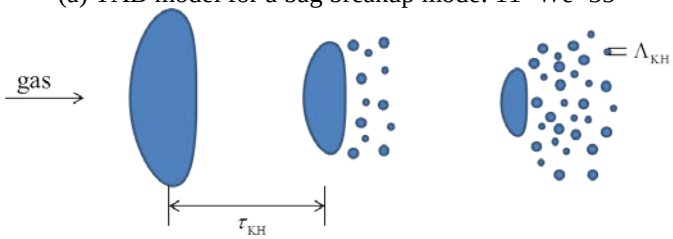

(b) KH model for a sheet-thinning breakup mode: 80<We<350

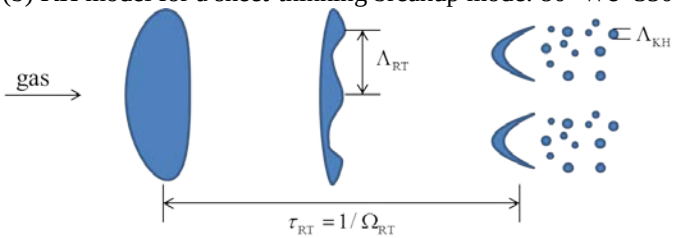

(c) KH/RT model for a catastrophic mode: We>350

Figure 2 Secondary Atomization Processes

The TAB model proposed by O'Rourke and Amsden [15] is based on the classical analogy between an oscillating and distorting droplet and a spring mass system. It is regarded that the external, restoring and damping forces in a spring mass system correspond to the drag, surface tension and viscous forces in a drop oscillation and distortion process. The TAB model defines a nondimensionalized droplet oscillation parameter to be $y = x/(C_b r)$ where x is the displacement of the droplet equator from its spherical position and C_b is a constant equal to 0.5. The droplet oscillation, y, can be expressed as Eq. (18) in terms of fluid properties and model constants solving Newton's 2nd law:

$$y(t) = We_c + e^{-(t/t_d)}\left[(y_0 - We_c)\cos(\omega t) + \frac{1}{\omega}\left(\frac{dy_0}{dt} + \frac{y_0 - We_c}{t_d}\right)\sin(wt)\right] \tag{18}$$

The breakup occurs when y>1 and the Sauter Mean Diameter (SMD) after breakup is determined by the energy balance as:

$$d_{32,c} = \frac{d}{1+\frac{8Ky^2}{20}+\frac{\rho_l r^3 \left(dy/dt\right)^2}{\sigma}\left(\frac{6K-5}{120}\right)} \tag{19}$$

The actual parcel size in the simulation is defined using a Rosin-Rommler distribution. Additionally the child drop after breakup is prescribed a velocity component normal to the parent drop velocity:

$$v_{normal} = C_v C_b r \frac{dy}{dt} \tag{20}$$

Reitz's breakup model is based on the Kelvin-Helmholtz instability phenomenon [16-18] and the results of the linear stability analysis are directly used in determining the important parameters in the atomization process. For easier use of the linear stability analysis results, the maximum growth rate, Ω, and corresponding wavelength, Λ, of the Kelvin-Helmholtz instability mode are expressed by curve-fits in terms of nondimensional numbers as:

$$\Omega_{\mathrm{KH}}\left[\frac{\rho_l a^3}{\sigma}\right]^{0.5} = \frac{\left(0.34+0.38\mathrm{We_g}^2\right)}{\left(1+\mathrm{Oh}\right)\left(1+1.4\mathrm{Ta}^{0.6}\right)} \tag{21}$$

$$\frac{\Lambda_{\mathrm{KH}}}{a} = 9.02\frac{\left(1+0.45\mathrm{Oh}^{0.5}\right)\left(1+0.4\mathrm{Ta}^{0.7}\right)}{\left(1+0.87\mathrm{We_g}^{1.67}\right)^{0.6}} \tag{22}$$

where We_g is the Weber number for the gas phase, $\mathrm{We_g} = \frac{\rho\left|\mathbf{U}-\mathbf{V}\right|^2 d}{\sigma}$, Oh is the Ohnesorge number, $\mathrm{Oh} = \nu_1\sqrt{\frac{\rho_l}{\sigma a}}$ and Ta is the Taylor parameter, $\mathrm{Ta} = \mathrm{Oh}\sqrt{\mathrm{We_g}}$. The liquid breakup is modeled by adding new child parcels and their size is determined by

$$r_c = B_0 \Lambda_{\mathrm{KH}} \tag{23}$$

where B_0 is a model constant and set equal to 0.61. Simultaneously, the parent drop size is reduced by

$$\frac{da}{dt} = -\frac{\left(a-r\right)}{\tau} \tag{24}$$

where τ is a time constant and determined from

$$\tau = 3.726 B_1 a / \Lambda_{\mathrm{KH}}\Omega_{\mathrm{KH}} \tag{25}$$

Child parcels are released when the stripped mass removed from the parent parcel exceeds a few percent of the average injected parcel mass. Newly formed parcels are assigned a random velocity direction within a confined cone angle defined by

$$\tan\left(\theta/2\right) = A_1 \Lambda_{\mathrm{KH}}\Omega_{\mathrm{KH}} / U \tag{26}$$

where A_1 = 0.188. In addition, as the parent parcel reduces in size, its mass is preserved by controlling the drop numbers contained in the parcel as $Na^3 = N_0 a_0^3$.

Lastly, the Rayleigh-Taylor (RT) model [16] is based on aerodynamic forces normal to the interface between two fluids that can drive the instability. Taking the external force acting on the droplet to be given by the aerodynamic drag, the acceleration can be expressed by dividing the drag force by the droplet mass:

$$a = \frac{3}{8} C_D \frac{\rho_g u_r^2}{\rho_l r} \tag{27}$$

Based on the linearized instability analysis by Chang, the wavelength and frequency of the fastest growing waves are determined as:

$$\Lambda_{\mathrm{RT}} = 2\pi\sqrt{\frac{3\sigma}{a\rho_l}} \tag{28}$$

$$\Omega_{\mathrm{RT}} = \sqrt{\frac{2a}{3}}\left[\frac{a\rho_l}{3\sigma}\right]^{1/4} \tag{29}$$

The droplet breakup is allowed to occur when the RT wavelength, Λ_{RT}, is smaller than the droplet diameter until the RT breakup time, $\tau_{RT} = 1/\Omega_{RT}$.

F. Eulerian-Lagrangian Coupling

Eulerian-Lagrangian coupling is accomplished through the source term vector, S, in Eq. (2). Mass, chemical species, momentum and energy transfer from the Lagrangian phase are provided as sources for the Eulerian phase:

$$S_L = \frac{d}{dt}\begin{pmatrix} \rho \\ \rho \mathbf{Y} \\ \rho \mathbf{V} \\ \rho h^0 - p \\ \rho \mathbf{K} \end{pmatrix} = \begin{pmatrix} \sum_N n\dot{m}_v \\ \sum_N n\dot{m}_v \\ \sum_N n\left(\dot{m}_v \mathbf{U} - m_l \dot{\mathbf{U}}\right) \\ \sum_N n\left(\dot{m}_v h_v - \dot{m}_v Q_d\right) \\ 0 \end{pmatrix} \tag{30}$$

where subscript *N* and *n* represent the number of parcels and the number of drops in an individual parcel respectively.

G. Computational Geometry, Mesh and Boundary Conditions

Three cases are considered in the present study at a given inlet air temperature and equivalence ratio as summarized in Table 2. In the three simulations, two different geometries are employed as shown in Figure 3. The full geometry contains all the major components in the combustor as indicated in Figure 3(a), where the y-axis scale is exaggerated to clearly illuminate the major components. The actual laboratory combustor configuration has a long length with a high aspect ratio as shown in Figure 3(b). The second geometry, given in Figure 3(c), is a reduced geometry, in which only a part of the air plenum and the combustor including the LDI element are considered. The main difference between the full and reduced geometries lies in the ability to support longitudinal acoustic modes in the combustor. The full geometry enables this by isolating the acoustic waves in the combustor by the insertion of a slotted inlet and an exit nozzle, whereas the reduced geometry is acoustically open.

Table 2 Summary of Cases Considered

Label	Tair	Φ	Geometry	Chemistry
Case 1	700 K	0.60	Reduced/Acoustically Open (Fig. 3 (c))	No Spray and Reaction
Case 2			Reduced/Acoustically Open (Fig. 3 (c))	Spray Combustion
Case 3			Full/Acoustically Closed (Fig. 3 (b))	Spray Combustion

In the simulation, all the surfaces of the geometry except for the inlet and exit planes are treated as no-slip and adiabatic walls. The inlet plane is located at the top left end of Figure 3 for the full geometry and left-end surface for the reduced geometry. The air flow enters through the inlet using a constant mass flow condition. At the exit nozzle located at the right-end surface, an outlet condition is imposed by a characteristic back pressure condition. The fuel spray is injected at the atomizer exit plane and the number of drops is specified in order to account for the correct fuel mass flow rate.

A hexahedral structured mesh system is used for the geometry as shown in Figure 4 and "butterfly" meshing is used for the circular cross-sections. A total of six million cells are employed for the full geometry and one million cells are used for the reduced geometry. According to our grid refinement studies using the full geometry, coarser meshes of one to two million cells are found to be incapable of properly resolving the acoustic oscillations.

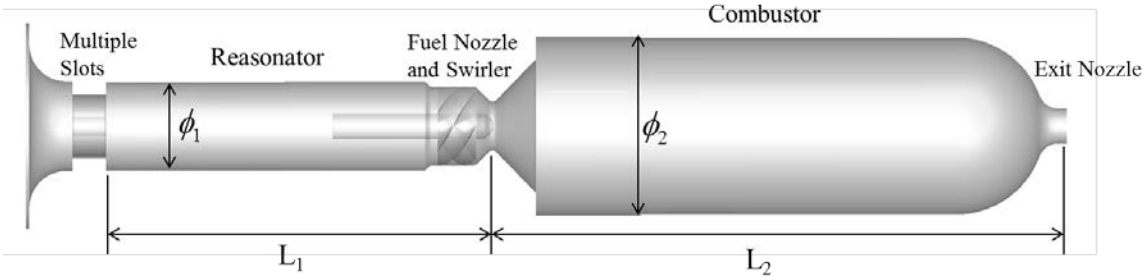

(a) Full combustor highlighting major components

(b) Full Combustor Geometry with 1:2 aspect ratio

(c) Acoustically-Open Combustor Geometry with 1:2 aspect ratio

Figure 3 Computational Domain of the laboratory LDI model combustor

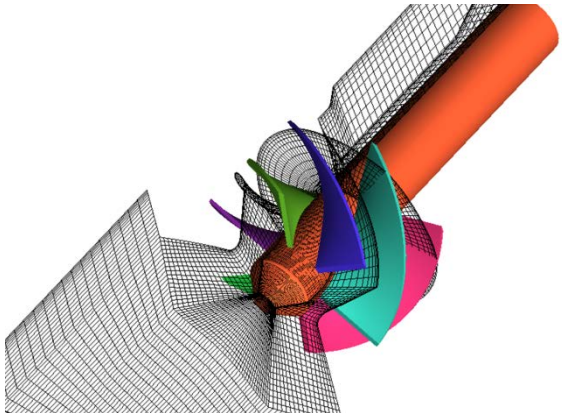

Figure 4 Computational Mesh visualized around the fuel nozzle and swirler

III. Decomposition Methods For Combustion Dynamics Diagnostics

To understand the underlying structure of the acoustic modes and the associated combustion dynamics, we utilize Dynamic Mode Decomposition (DMD) techniques. DMD takes an ensemble of data, either instantaneous or a series of snapshots, as inputs and uses the Arnoldi algorithm (for DMD) to define 'modes' that are mathematically orthogonal to each other. A detailed mathematical description of the DMD approach can be found in Rowley et al. [19] and Schmid [20]. Here, the mathematical model is briefly reviewed.

A. Mathematical Model of DMD

We wish to approximate a function $z(x,t)$ over some domain of interest as a finite sum in the variables-separated form

$$z(x,t) \approx \sum_{k=1}^{M} a_k(t)\Phi_k(x) \tag{31}$$

with a reasonable expectation that the approximation becomes exact as M approaches infinity, except possibly on a set of measure zero. Note that in Eq. (31) there is no fundamental difference between x and t, but we usually think of x as a spatial coordinate (1D, 2D & 3D vector-valued) and t as the temporal coordinate.

The representation of Eq. (31) is not unique. For example, if the domain (experimental or computational) is a bounded interval X on the real line, then the functions $\Phi_k(x)$ can be chosen as a Fourier series, or Legendre polynomials, or Chebyshev polynomials, and so on. For different selections of the space-dependent function, $\Phi_k(x)$, the corresponding time-dependent function, $a_k(t)$, will be different. They can be periodic or non-periodic, single-frequency dominated or multi-frequency dominated.

In the POD analysis, the spatial functions, $\Phi_k(x)$, are chosen to be orthonormal functions, i.e.

$$\int_X \Phi_{k_1}(x)\Phi_{k_2}(x)dx = \begin{cases} 1 \text{ if } k_1 = k_2 \\ 0 \text{ otherwise} \end{cases} \tag{32}$$

Then

$$a_k(t) = \int_X z(x,t)\Phi_k(x)dx, \tag{33}$$

From Eq. (32) and (33), it is noted that given that $\Phi_k(x)$ is selected to be orthonormal, the determination of $a_k(t)$ will be only dependent on $\Phi_k(x)$ rather than on the other Φ s.

B. Arnoldi Algorithm

In DMD analysis, in order to obtain single frequency dynamic modes, linear mapping is assumed from one snapshot to another. Suppose the dataset is represented as a snapshot sequence,

$$V_1^N = \{v_1, v_2, v_3, ..., v_N\} \tag{34}$$

where v_i stands for the i^{th} flow field and $v_{i+1} = Bv_i$. The matrix B here represents the linear mapping matrix. Therefore,

$$V_1^N = \{v_1, Bv_1, B^2v_1, ..., B^{N-1}v_1\} \tag{35}$$

Another assumption is that there exists a specific number *N*, beyond which the vector v_N can be expressed as linear combination of the previous vectors,

$$v_1 = a_1v_1 + a_2v_2 + ... + a_{N-1}v_{N-1} \quad \text{or} \quad v_1 = V_1^{N-1}a + r \tag{36}$$

Hence,

$$BV_1^{N-1} = V_2^N = V_1^{N-1}S + re_{N-1}^T \tag{37}$$

where,

$$S = \begin{pmatrix} 0 & & & a_1 \\ 1 & 0 & & a_2 \\ & \ddots & \ddots & \vdots \\ & & 1 & 0 & a_{N-2} \\ & & & 1 & a_{N-1} \end{pmatrix} \tag{38}$$

Applying the eigen-value decomposition for matrix *S*,

$$S = T^{-1}\Lambda T \tag{39}$$

where matrix *T* is the eigen-vector matrix of *S*. Suppose a sufficient number of snapshots are used, the eigenvalues of *S* can very well represent the eigenvalues of *A*, which contains the time-evolution information of the flow field. Also, the dynamic modes corresponding to single frequency response can be constructed as,

$$\Phi = V_1^{N-1}T^{-1} \tag{40}$$

Similarly, the original data set can be decomposed into the form in Eq. (31),

$$V_1^{N-1} = \Phi T \tag{41}$$

where matrix Φ contains the dynamic spatial information and matrix *T* contains the temporal evolutional information.

IV. Results

The diverse physics in the combustor and their coupling mechanisms are investigated by a series of combustion dynamics simulations, which illuminate the roles of hydrodynamics, spray formation, heat release, and acoustics. The cases listed in Table 2 are designed to focus on the specific flow physics of interest. For example, Cases 1 and 2 show how the flow characteristics are influenced by chemical reactions, especially the combustion heat release. On the other hand, Case 3 isolates the acoustics effects that are the result of the acoustically closed environment. In all cases, the acoustic characteristics from the computational results are compared with those from the companion experimental study.

A. Dynamic Flow Characteristics

A large central toroidal recirculation zone (CTRZ) is found in time-averaged results in both the non-reacting and reacting flow cases as shown in Figure 5. The CTRZ shows the presence of asymmetric, unsteady spiral motion. This behavior is commonly found in swirling flows and is associated with self-excited hydrodynamic flow instabilities referred to as precessing vortex core (PVC) instabilities. The strong swirling flow generated by the swirler vane has radial gradients of the azimuthal velocity and pressure. As the flow is expanded continuously in the venturi-diverging section and subsequently at the combustor backstep, there is a corresponding decay of the azimuthal velocity and the radial pressure gradients. In turn, this leads to a reversal in the axial pressure gradient which results in the formation of the CTRZ. Since the axial decay of azimuthal momentum and radial pressure gradient forms the CTRZ structure, the combustor head geometry and flow conditions can be critical factors in determining the size and strength of CTRZ. The PVC instabilities occur when the CTRZ becomes unstable and asymmetric. A series of self-excited vortices is apparent in the planar view of the combustor head region shown in Figure 6. The vortices are generated at the nozzle exit and merge into the main recirculation zone (frames b to d). This process alternates during the PVC time period, inducing an asymmetric vortex structure.

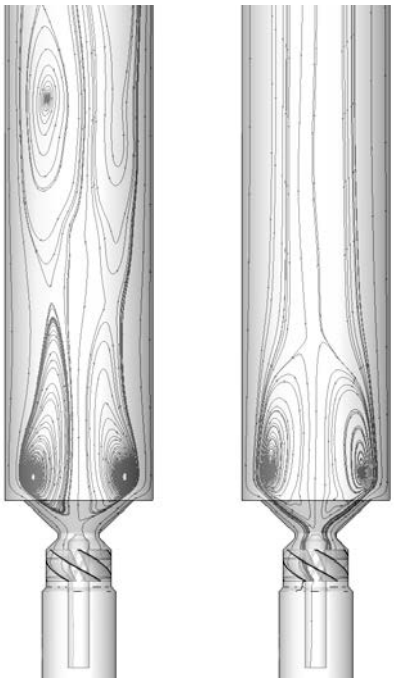

Figure 5 Time-averaged streamlines: non-reacting flow (left) and reacting flow (right)

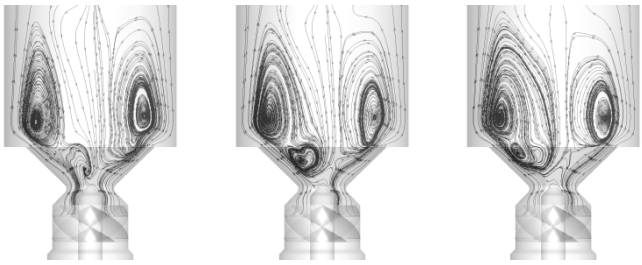

(a) $t = t_0$ (b) $t = t_0 + 1/6\ \tau_{PVC}$ (c) $t = t_0 + 2/6\ \tau_{PVC}$

(d) $t = t_0 + 3/6\ \tau_{PVC}$ (e) $t = t_0 + 4/6\ \tau_{PVC}$ (f) $t = t_0 + 5/6\ \tau_{PVC}$

Figure 6 Instantaneous streamlines during a PVC mode period

The main difference between non-reacting and reacting flows is the existence of a secondary downstream vortical structure in the non-reacting case. The volume expansion of the gas due to combustion allows the main recirculation zone to fill a larger region at the chamber head. The main recirculation zone then serves as a blockage for the swirling air flow, the mean flow speed at the outer shear layer is accelerated. This increased axial momentum in turn leads to the straight flow-through pattern observed beyond the CTRZ in the reacting flow case. In addition, the expansion of CTRZ and the acceleration of the air flow also leads to a shifting of the PVC frequency to higher values. The distinct frequencies are obtained using the DMD method and are summarized in Table 4, indicating a frequency shift of about 15% between Case 1 (non-reacting) and Case 2 (reacting).

Table 3 Comparison of hydrodynamic modes for non-reacting and reacting flows

Hydrodynamic Mode	Non-reacting Flow (Hz)	Reacting Flow (Hz)
PVC (fundamental)	3049	3505
PVC (2nd harmonic)	6177	7075
PVC (3rd harmonic)	9304	10580
PVC (4th harmonic)	12353	14213

B. Spray and combustion characteristics

In the present combustion dynamics simulation, the flame seems to be strongly influenced by the hydrodynamics of the swirling air flow. In Figure 7, which shows the time-averaged heat release contours, the flame starts from the stagnation point of CTRZ and follows the outer shear layer until the combustor head. Further, the flame surface also fluctuates due to the PVC instabilities. A series of shed vortices distorts the outer shear layer and the resulting flame.

The fuel spray is finely atomized in the diverging section of the venturi as shown in Figure 8, with a D_{32} ranging from 30 to 40 μm. The high pressure condition rapidly promotes secondary atomization and the subsequent vaporization rate of droplets. It is important to note that the strong intensity of heat release is enhanced by the secondary atomization and is potentially an important mechanism for the excitation of combustion instability.

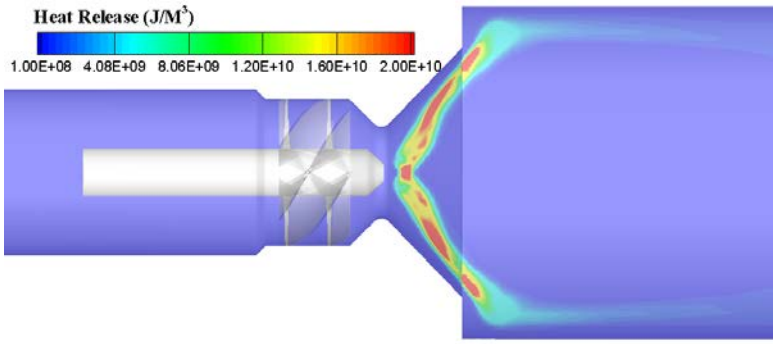

Figure 7 Time-averaged heat release contour

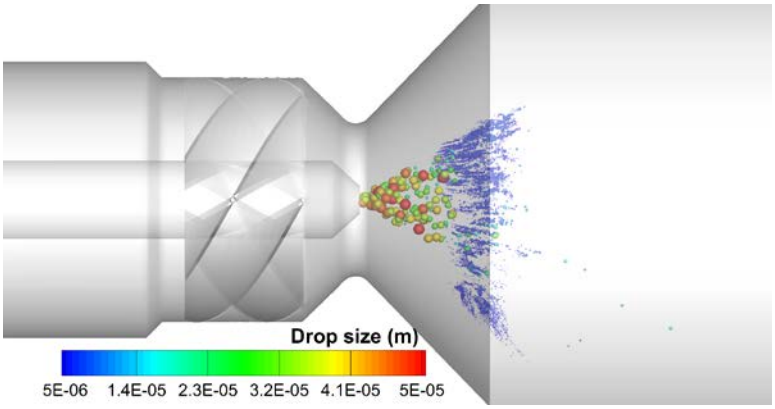

Figure 8 Instantaneous spray drops colored by size

C. Modal Analysis in an Acoustically-Open Combustor

Modal analysis was conducted using PSD's based on the wall pressure at the chamber head as shown in Figure 9. It can be observed that the pressure oscillation levels are amplified in the presence of chemical reactions. The pressure amplitude is 0.2 kPa for the non-reacting flow case, whereas it is 0.6 kPa for the reacting flow case. The maximum oscillation amplitude was 6 kPa around the LDI element where the PVC instability occurs. In fact, the PVC instability appears to be a key driver of the pressure oscillations in both cases. In the non-reacting case, although the PVC instability has no direct mechanism for generating the acoustic perturbations, the results indicate a weak intensity pressure perturbations corresponding to the PVC modes. In the reacting flow case, there are several distinct pressure peaks in the PSD plot, which can be further investigated using DMD analysis.

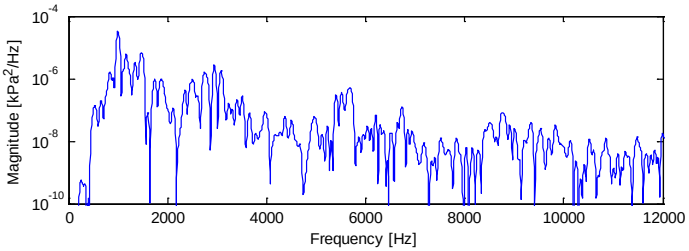

(a) non-reacting flow

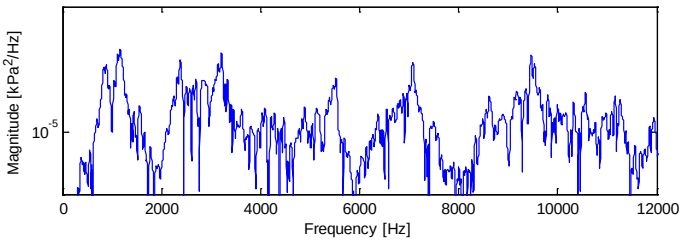

(b) reacting flow

Figure 9 Wall Pressure PSDs for acoustically-open combustor

Using the DMD analysis, the mode power spectrum based on the pressure over the entire flow field is obtained as shown in Figure 10. Strong harmonic PVC peaks are dominant features in the non-reacting flow case. Additional pressure peaks appear in the mode power spectrum in the reacting flow case. Longitudinal acoustics are involved even in an acoustically-open chamber geometry because the exit boundary is not a perfect non-reflecting boundary condition. Moreover, a tangential acoustic mode is apparent at 9433 Hz. In addition, a spinning mode and associated higher harmonics are observed at 510, 1020 and 1530 Hz in the DMD spectrum for the azimuthal vorticity, as seen in Figure 11. The major mode shapes obtained from the DMD analysis are illustrated in Figure 12. The results clearly indicate that the flows at the combustor head and in the venturi diverging section are strongly influenced by the PVC instability and the swirl spinning mode.

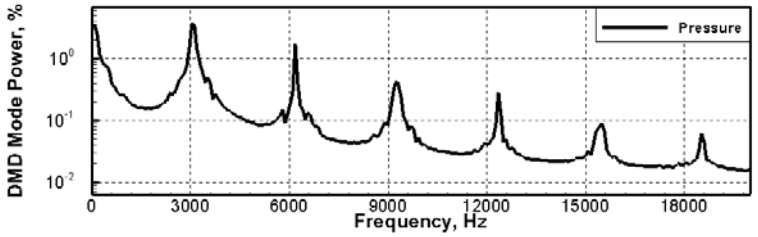

(a) non-reacting flow

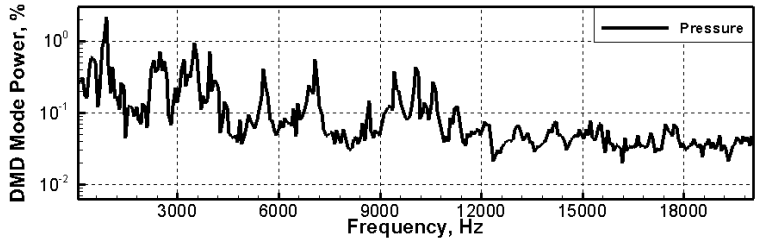

(b) reacting flow

Figure 10 DMD Mode Power Spectrum for Pressure

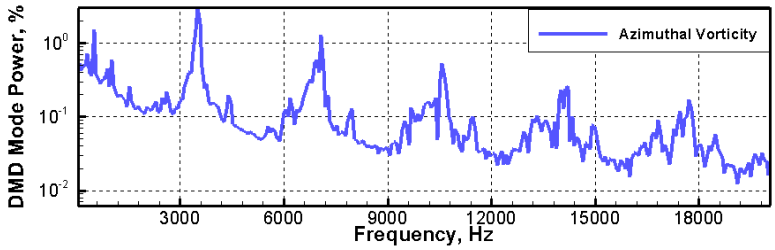

Figure 11 DMD Mode Power Spectrum for Azimuthal Vorticity in Reacting Flow

Table 4 Summary of DMD Modes and Corresponding Frequencies

DMD Mode	Frequency (Hz)
Unknown mode	892
Spinning mode (1, 2, and 3)	510, 1020 and 1530
PVC mode (1, 2 and 3)	3505, 7075 and 10580
Longitudinal mode (1L, 2L and 3L)	2486, 3952 and 5545
Tangential mode (1T)	9433

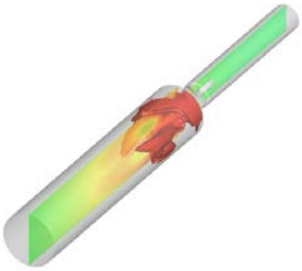

a) Spinning mode (510 Hz)

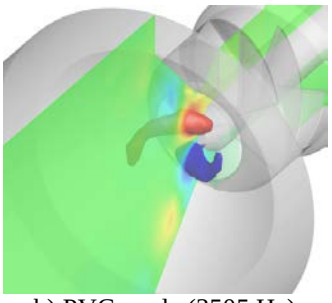

b) PVC mode (3505 Hz)

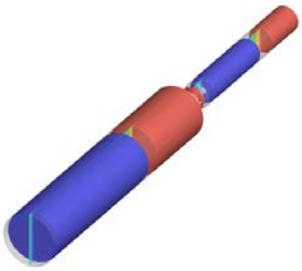

c) 1L

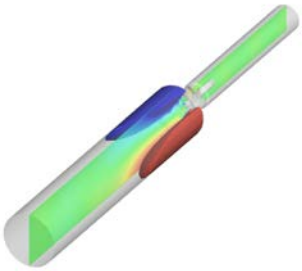

d)1T

Figure 12 DMD Mode Shapes for Pressure in an Acoustically-Open Chamber

D. Estimation of Self-Excited Combustion Instability

Self-excited combustion instabilities are observed in the acoustically-closed combustor flow simulations. In thic ase, the present simulations are preliminary in nature and did not include the full atomization models as described in Section 2.E. Instead, the primary atomization model was neglected and the injected drop diameter was assumed to be equal to the liquid sheet thickness obtained from the Eulerian VOF simulation for the atomizer free surface flow. Moreover, the secondary atomization model was restricted to the Kelvin-Helmholtz model. Due to the small injected droplet sizes, secondary atomization effects are not strong. However, as indicated in Figure 13, the qualitative trends in the PSD plots are consistent with the experimental results. Both simulations and experiments show evidence of a strong 4L mode and a second 6000 Hz peak as discussed in the next section.

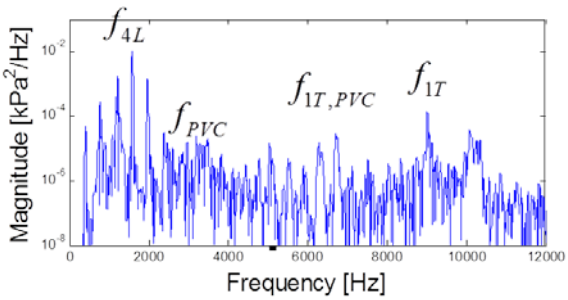

(a) Computation

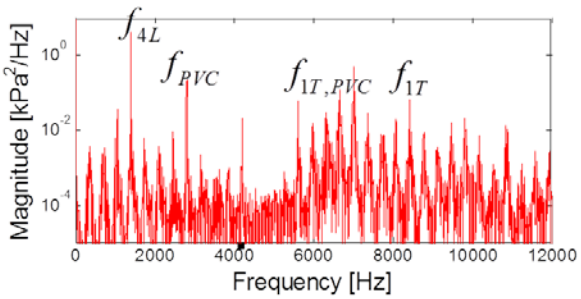

(b) Experiments

Figure 13 Wall Pressure PSDs for acoustically-closed combustor

E. Nonlinear PVC-Acoustic Couplings and Feedback Loop

The dominat 4L and 6000 Hz modes observed in the acoustically closed results arise from non-linear interactions between hydrodynamics and acoustics modes. Experiments in lean premixed swirl combustors have also indicated the presence of such interactions. A hypothesis regarding nonlinear PVC-acoustics coupling can be developed using a Rayleigh criterion-based analysis in the frequency domain. Our approach uses the acoustic energy equation written as:

$$\frac{\partial}{\partial t}\left[\frac{p'^2}{2\rho c^2}+\frac{\rho u'^2}{2}\right]+\frac{\partial}{\partial x}\left(p'u'\right)=\left[\frac{\gamma-1}{\gamma}p'Q'\right] \tag{42}$$

where, if we note that the pressure perturbation typically originates from the acoustics and while the unsteady heat release is largely influenced by the PVC modes. The pressure and heat release perturbations can therefore be expressed as:

$$p' = \hat{p}e^{i\omega_a t} \;\square\; \hat{p}\cos\left(\omega_a t\right) \tag{43}$$

$$Q' = \hat{Q}e^{i\omega_{PVC} t} \;\square\; \hat{Q}\cos\left(\omega_{PVC} t+\phi\right) \tag{44}$$

It is important to note the nonlinear pressure-heat release coupling term on the right hand side of Eq. (42). This term leads to two interactive frequencies which can be identified as:

$$\begin{aligned} p'Q' &= \hat{p}\hat{Q}\cos\left(\omega_a t\right)\cos\left(\omega_{PVC} t+\phi\right) \\ &= \frac{\hat{p}\hat{Q}}{2}\left\{\cos\left[\left(\omega_a+\omega_{PVC}\right)t+\phi\right]+\cos\left[\left(\omega_a-\omega_{PVC}\right)t-\phi\right]\right\} \end{aligned} \tag{45}$$

The sum and minus of two driving frequencies can thus be produced by this nonlinear pressure-heat release coupling process. In the LDI combustor, the two driving frequencies are the acoustics and hydrodynamics, which in turn produce two interactive modes.

Another noteworthy result is the establishment of a feedback loop arising from this nonlinear interaction. The interactive modes can the couple with other existing modes such as the longitudinal and tangential acoustic modes and the PVC modes. If we consider PVC-4L (3200 Hz/1600 Hz) coupling, the interactive modes are 4800 Hz and 1600 Hz. 1600 Hz is the 4L mode and the PVC-4L interaction leads to further 4L mode amplification. In addition to PVC-4L coupling, a strong PVC-1T (3200 Hz - 9600 Hz) coupling can produce interactive modes at 12800 Hz and 6400 Hz. Here, the 6400 Hz mode is the second harmonic of PVC which can also form a feedback loop, too. Based on this approach, we can estimate that the 1600 Hz (4L, PVC-4L) and 6400 Hz (2PVC, PVC-1T) are the dominant interaction modes, which agrees well with strong peaks observed in the PSD in Figure 13.

In summary, the combustion dynamics mechanism in the LDI combustor can be attributed to nonlinear interactions between the hydrodynamics, chamber acoustics, and combustion as shown in Figure 14. Strong hydrodynamic modes such as the PVC instabilities can influence the flame dynamics and, in turn, the acoustics. The unsteady heat release from the flame and pressure perturbation from the acoustics produces two interactive modes. When these interactive modes are associated with existing hydrodynamic or acoustic modes, a feedback loop is established which can give rise to the excitation of combustion instability.

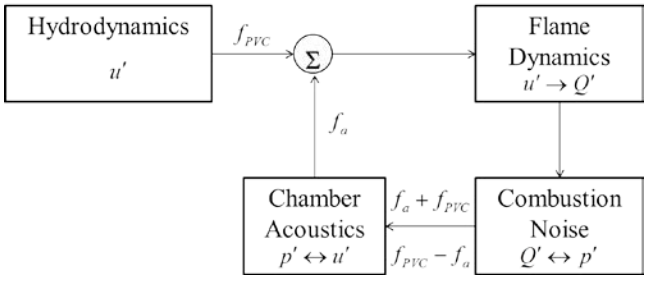

Figure 14 Schematics of Combustion Dynamics Mechanism in a LDI Combustor

V. Conclusions

Self-excited combustion instabilities are computationally investigated for the LDI gas turbine combustor. Three simulations are considered in the present investigation: non-reacting and reacting flows in an acoustically open chamber and reacting flow in an acoustically closed chamber. Findings from simulations can be summarized as:

- Dynamic flows appear in both non-reacting and reacting flows. PVC instabilities represent key hydrodynamics phenomena in the LDI combustor and the spray and the flame respond strongly to these instabilities.
- Self-excited combustion instabilities are captured successfully in the simulations and the dominant peaks in PSD agree well with those in the experimental results.
- A hypothesis about the underlying combustion dynamics mechanism in a LDI gas turbine combustor has been presented, wherein the key driver is the nonlinear interaction between the PVC-related heat-release modes and the acoustics modes. We argue that the presence of a feedback loop may lead to the excitation and sustenance of combustion instabilities.

Acknowledgments

The authors acknowledge the support of the NASA Glenn Research Center and Program Manager Mr. Kevin Breisacher in sponsoring the subjet work under NASA Research Announcement (NRA) grant number NNX11AI62A. Also, we would like to give special thanks to Drs. Charles Merkle and Hukam Mongia who set the original direction of the study and Dr. Phil Lee ofWoodward for providing the fuel nozzle used in the experiment.

References

[1] T. Yi and E. J. Gutmark, "Stability and Control of Lean Blowout in Chemical Kinetics-Controlled Combustion Systems," *Combustion Science and Technology,* vol. 181, pp. 226-244, 2009 2009.

[2] M. S. Howe, "The Dissipation of Sound at an Edge," *Journal of Sound and Vibration,* vol. 70, pp. 407-411, 1980 1980.

[3] D. Li, G. Xia, V. Sankaran, and C. L. Merkle, "Computational Framework for Complex Fluid Physics Applications," in *Computational Fluid Dynamics 2004*, ed: Springer Berlin Heidelberg, 2006, pp. 619-624.

[4] X. Guoping, S. Venkateswaran, L. Ding, and M. Charles, "Modeling of Turbulent Mixing Layer Dynamics in Ultra-High Pressure Flows," in *36th AIAA Fluid Dynamics Conference and Exhibit*, ed: American Institute of Aeronautics and Astronautics, 2006.

[5] R. Smith, M. Ellis, G. Xia, V. Sankaran, W. Anderson, and C. L. Merkle, "Computational Investigation of Acoustics and Instabilities in a Longitudinal-Mode Rocket Combustor," *Aiaa Journal*, vol. 46, pp. 2659-2673, Nov 2008.

[6] F. Thomas, H. Matthew, M. Charles, and A. William, "Comparison Between Simulation and Measurement of Self-Excited Combustion Instability," in *48th AIAA/ASME/SAE/ASEE Joint Propulsion Conference & Exhibit*, ed: American Institute of Aeronautics and Astronautics, 2012.

[7] M. E. Harvazinski, W. E. Anderson, and C. L. Merkle, "Analysis of Self-Excited Combustion Instabilities Using Two- and Three-Dimensional Simulations," *Journal of Propulsion and Power,* vol. 29, pp. 396-409, 2013/06/11 2013.

[8] D. Basu, A. Hamed, K. Das, and Asme, "DES, hybrid RANS/LES and PANS models for unsteady separated turbulent flow simulations," *Proceedings of the ASME Fluids Engineering Division Summer Conference, Vol 2*, pp. 683-688, 2005 2005.

[9] R. A. Baurle, C. J. Tam, J. R. Edwards, and H. A. Hassan, "Hybrid Simulation Approach for Cavity Flows: Blending, Algorithm, and Boundary Treatment Issues," *AIAA Journal*, vol. 41, pp. 1463-1480, 2013/03/29 2003.

[10] C. K. Westbrook and F. L. Dryer, "Simplified Reaction-Mechanisms for the Oxidation of Hydrocarbon Fudels in Flames," *Combustion Science and Technology*, vol. 27, pp. 31-43, 1981 1981.

[11] A. Putnam, "Integratable Form of Droplet Drag Coefficient," *American Rocket Society Journal,* vol. 31, pp. 1467-1468, 1961.

[12] G. M. Faeth, "Evaporation and Combustion of Sprays," *Progress in Energy and Combustion Sciences*, vol. 9, pp. 1-76, 1983.
[13] I. Ashraf and M. A. Jog, "Nonlinear breakup model for a liquid sheet emanating from a pressure-swirl atomizer," *Journal of Engineering for Gas Turbines and Power-Transactions of the Asme*, vol. 129, pp. 945-953, Oct 2007.
[14] P. K. Senecal, D. P. Schmidt, I. Nouar, C. J. Rutland, R. D. Reitz, and M. L. Corradini, "Modeling high-speed viscous liquid sheet atomization," vol. 25, pp. 1073-1097, 1999/11// 1999.
[15] P. J. O'Rourke and A. A. Amsden, "The Tab Method for Numerical Calculation of Spray Droplet Breakup," 1987.
[16] J. C. Beale and R. D. Reitz, "Modeling spray atomization with the Kelvin-Helmholtz/Rayleigh-Taylor hybrid model," *Atomization and Sprays*, vol. 9, pp. 623-650, Nov-Dec 1999.
[17] Z. Y. Han, S. Parrish, P. V. Farrell, and R. D. Reitz, "Modeling atomization processes of pressure-swirl hollow-cone fuel sprays," *Atomization and Sprays*, vol. 7, pp. 663-684, Nov-Dec 1997.
[18] M. A. Patterson and R. D. Reitz, "Modeling the effects of fuel spray characteristics on diesel engine combustion and emission," 1998.
[19] C. W. Rowley, I. Mezic, S. Bagheri, P. Schlatter, and D. S. Henningson, "Spectral analysis of nonlinear flows," *Journal of Fluid Mechanics*, vol. 641, pp. 115-127, Dec 25 2009.
[20] P. J. Schmid, "Dynamic mode decomposition of numerical and experimental data," *Journal of Fluid Mechanics*, vol. 656, pp. 5-28, Aug 10 2010.